ELSEVIER

Contents lists available at ScienceDirect

Ocean Engineering

journal homepage: www.elsevier.com/locate/oceaneng



Research paper

Non-causal model predictive control for rigid-body wave energy converters based on physics-informed neural networks

Vincentius Versandy Wijaya^a, Yao Zhang^{b,*}

- ^a School of Engineering, University of Southampton, Southampton, SO16 7QF, UK
- ^b Department of Mechanical Engineering, University College London, London, WC1E 7JE, UK

ARTICLE INFO

Physics-informed machine learning

Keywords: Physics-informed neural networks (PINNs) Model predictive control (MPC) Energy maximisation Wave energy converters (WECs)

ABSTRACT

The energy maximisation for Wave Energy Converters (WECs) is a non-causal problem where the current power take-off (PTO) force incorporates knowledge of future wave prediction to significantly boost energy harnessing. Since WECs are constrained by PTO limitation and other limitation regarding safe operations, model predictive control (MPC), as a well-known non-causal control algorithm, is considered as a proper algorithm to optimise the energy output subject to multiple constraints. However, MPC controller relies on an accurate model to generate maximum energy. Obtaining and utilising such fully known models is challenging due to the highly nonlinear dynamics and stochastic sea wave environment of WECs in various wave conditions. Traditional machine learning method can be a solution since they are able to model complex dynamical systems. However, they suffer from the requirement of a large amount of training data, which introduces significantly increased computational burden. To tackle these challenges, this paper introduces a control framework that can utilise prior partial model information and have better sampling efficiency by integrating Physics-Informed Neural Networks (PINNs) with MPC to optimise the energy generation of WECs. As the benchmark of WECs control, the point absorber is chosen to evaluate the effectiveness of the proposed PINNs-MPC, in which 35 sea wave scenarios ranging from $H_s = 1.25$ m, $T_p = 1$ s to $H_s = 2.50$ m, $T_p = 1$ s are tested. The proposed method can be applied to other types of WECs by retaining the PINNs.

1. Introduction

Ocean waves present a significant potential source of sustainable energy. Global estimates suggest that wave energy can generate up to 29,500 TWh annually (Trust, 2014), with 40-50 TWh/year (Trust, 2012) potentially exploitable within the UK. To harness wave energy, various wave energy converters (WECs) have been developed, including point absorbers (Erselcan and Kükner, 2020), attenuators (Liao et al., 2023), and oscillating water columns (Rosati et al., 2022). Despite its potential, wave energy technology is still less mature compared to the more established wind and solar energy sectors. (Jin and Greaves, 2021). Commercialisation faces challenges, particularly due to the high levelised cost of energy (LCoE), which reached approximately £300/MWh in 2018 (Smart and Noonan, 2018). To address these challenges, the International Energy Agency (IEA) has developed a strategic roadmap to harness the potential of wave energy, aiming to achieve a generation capacity of 180 GW by 2050 (Systems, 2023). Similarly, within the UK, Engineering and Physical Sciences Research Council (EPSRC) released the Wave Energy Road Map in 2020 (EPSRC, 2020), outlining the pathway

to reduce the LCoE to £90/MWh by 2035 and achieve an installed capacity of 22 GW by 2050. One of the critical components in achieving these targets involves the development of advanced control strategies aimed at reducing costs and enhancing the survivability of WECs systems.

Control strategies have long been recognised as critical in optimising the energy output of WECs. Early control methods, such as complex conjugate (Budal and Falnes, 1980), latching (Feng and Kerrigan, 2013), and declutching (Feng and Kerrigan, 2015), were designed to match the natural frequency of the device with the dominant frequency of the incoming waves to induce resonance. Although these control approaches are simple to implement under regular wave conditions, they become less effective when incident waves contain multiple frequencies (Babarit and Clément, 2006). Furthermore, these early methods often fail to account for the physical limitations of the WECs (Faedo et al., 2017), leading to excessive resonance motion, which can damage the device and shorten its operational life. Despite their limitations, these methods have remained in use in the recent years, primarily because of their simplicity and low computational complexity (Barone et al., 2024; Liu et al., 2021; Yu et al., 2024).

E-mail addresses: Vincentius.Versandy.Wijaya@soton.ac.uk (V.V. Wijaya), Yao.Zhang@ucl.ac.uk (Y. Zhang).

^{*} Corresponding author.

To effectively handle constraints in control systems, Model Predictive Control (MPC) has been widely acknowledged as a mature technique. MPC, an optimization-based control strategy, solves constrained optimal control problems, and its application in WECs control has been extensive (Zhang et al., 2024a; Lin et al., 2023; Zhan et al., 2023; Kaiser et al., 2025). However, achieving optimal control through MPC requires accurate future wave information, and thus it is a non-causal control problem. A range of wave prediction techniques have been developed, including well-established methods such as Deterministic Sea Wave Prediction (Belmont et al., 2014), Adaptive Sliding Mode Observer to cope with model uncertainty (Zhang et al., 2020a, 2021), as well as more recent machine learning approaches, for example, Long Short-Term Memory (LSTM) networks (Meng et al., 2022) and Gaussian Processes (GP) (Shi et al., 2018). These techniques can be readily incorporated into MPC frameworks to enhance energy conversion efficiency.

Beyond wave prediction, recent applications of machine learning to WECs control have emerged. Techniques such as reinforcement learning (Zou et al., 2022; Wang et al., 2024) and supervised learning (Zhang et al., 2024b; Pasta et al., 2021) have demonstrated their effectiveness to WECs control. Supervised learning, in particular, can construct WECs models as neural networks (NNs) based on experimental or simulation data. However, traditional machine learning methods suffer from issues related to sampling efficiency and the lack of model interpretability. To address these challenges, a novel deep learning method, Physics-Informed Neural Networks (PINNs), was proposed by (Raissi et al., 2019). The main idea of PINNs is to incorporate prior physical information to the network via an additional loss function. This can be evaluated using unlabelled datapoints, reducing the need for large amounts of labelled data. In addition, this approach imposes constraints on the NNs to adhere to known physical laws, enhancing the model's interpretability. The application of PINNs has been demonstrated in various fields, including turbulent flows (Jin et al., 2021), heat transfer (Cai et al., 2021), and biophysics (Zapf et al., 2022).

Recent studies have explored the integration of PINNs with MPC to improve control performance, especially in cases where model development requires costly simulations or experiments. It has been extensively studied in tracking problems, such as in multi-link robotic systems (Nicodemus et al., 2022), autonomous underwater vehicles (Liu et al., 2024), and process control (Zheng et al., 2023). In these researches, PINNs-MPC provides superior tracking performance compared to conventional NNs models. Other study highlights the strength of PINNs-MPC to generalise beyond the small-labelled dataset (Zheng et al., 2023). However, to the best of the authors' knowledge, the use of PINNs-MPC to optimise energy generation has not yet been explored. Therefore, this study is the first attempt to address this gap by applying the PINNs-MPC framework, and this is the first attempt to utilise PINNs to solve the energy maximisation problem of WECs. The contributions of this paper are summarised as follows:

- 1. This paper is the first attempt to propose PINNs-MPC scheme to tackle the unique challenges of WECs, which are multiple constraints, external disturbances, and partially-known model.
- The proposed PINNs-MPC scheme is designed to maximise the energy output of WECs with future wave height information incorporated into the scheme.
- 3. The superior sampling efficiency of PINNs is demonstrated in comparison to the conventional NNs for the WECs application.
- 4. Comprehensive comparison study is conducted between the proposed PINNs-MPC scheme, conventional NNs-MPC, and traditional MPC that assumes perfect and imperfect knowledge of the system in irregular wave conditions and real-world wave conditions.
- The study utilised real-world wave height data collected from the coast of Cornwall, UK, for the validation and testing of the proposed control scheme.

The remainder of this paper is organised as follows. Section 2 provides the problem statement of maximising energy output for WECs con-

trol. Section 3 introduces PINNs and implementation of the proposed PINNs-MPC algorithm. In Section 4, the result of the model training is presented, as well as the performance of the system in both the open-loop and the closed-loop simulations. Finally, Section 5 concludes the paper and outlines the future works.

2. WECs control problem statement

In this section, the problem statement for the WECs optimal energy generation control is introduced. In WECs system, the target of a controller is to produce maximum energy while satisfying physical constraint and limitation in control input. This can be formulated as constrained finite-horizon optimisation in discrete time with sampling time (T_s) as follows.

$$\begin{aligned} & \underset{u(\cdot)}{\min} \quad J_N(x_0, u(\cdot)) := \sum_{k=0}^{N-1} l(x_k, u_k) \\ & \text{s.t.} \quad x_{k+1} = \phi(T_s, x_k, u_k, w_k), \\ & \quad x_k \in \mathbb{X}, \quad u(\cdot) = \left\{ u_0, \dots, u_{N-1} \right\} \in \mathbb{U}, \\ & \quad x_{k-0} = x_0 \end{aligned} \tag{1}$$

where ϕ is the model defined by PINNs (see Remark 1), N is the prediction horizon, x_0 is the initial condition at timestep k. x_k , w_k , u_k are the discrete states, wave height, and control input at timestep k, and with the cost function

$$l(x_k, u_k) := x_k^T Q x_k + u_k^T r u_k + u_k \dot{z}_k$$
 (2)

where the first two terms, $x_k^T Q x_k + u_k^T r u_k$, aim to penalise states and control input, Q and r are the weighing matrix that can be tuned to influence this penalisation. To maximise energy generation, this paper maximises the power absorbed by the power take-off (PTO) with the third term, $u_k \dot{z}_k$.

The optimisation in Eq. (1) requires N-1 steps ahead future wave information. In each timestep, the optimisation generates the control input from the first element of $u(\cdot)$, which is applied to the system. The state is then updated from the real system, and the optimisation is performed again for the following timestep. The dynamic equality constraint in Eq. (1) is determined by PINNs (ϕ) while the state and control input constraints are defined as follows

$$\mathbb{X} := \left\{ x \in \mathbb{R}^{n_x} : |x_1| \le z_{max}, \quad |x_2| \le \dot{z}_{max} \right\},
\mathbb{U} := \left\{ u \in \mathbb{R} : |u| \le u_{max} \right\}$$
(3)

where $z_{\rm max}$, $\dot{z}_{\rm max}$, $u_{\rm max}$ are the maximum limit of displacement, velocity, and control input respectively, and n_x is the number of states. This limit is placed to increase the survivability and prolonged the service life of the device. The optimisation in Eq. (1) is a nonlinear programming problem since the dynamic model defined by PINNs is nonlinear. This can be solved by mature Sequential Quadratic Programming and Interior Point technique (Frison and Diehl, 2020; Wächter and Biegler, 2006)

Remark 1. Compared to the traditional MPC, the scheme in Eq. (1) uses PINNs as the prediction model. This is explicitly stated in the dynamic equality constraint. In WECs problem, the advantage of utilising such prediction model is that PINNs are known to be sample efficient. Therefore, in the case of lacking expensive experimental data and high-fidelity simulation, PINNs can help improving the accuracy of the model with the help of prior physical knowledge. Nonetheless, there are challenges in the training process due to the addition of physical knowledge, and more discussions can be found in Rathore et al. (2024)

Remark 2. The cost function in Eq. (2) is constructed to optimise energy generation by an additional term, $u_k \dot{z}_k$. This is different compared to other existing PINNs-MPC schemes that focus on the trajectory tracking and regulation problem (Liu et al., 2024; Nicodemus et al., 2022).

Remark 3. The cost function in Eq. (2) is formulated to maximise mechanical power which is a common objective function in WEC control

studies (Faedo et al., 2017; Ringwood et al., 2014). However, mechanical power objective function can be transformed into electrical objectives by considering the efficiency term due to the generator, hydraulic transmission, and inverters as outlined in Tona et al. (2015)

3. Model predictive control-based physics-informed neural networks

In this section, the PINNs and MPC frameworks are presented along with an explanation of the implementation of the algorithm.

3.1. Physics-informed neural networks (PINNs)

PINNs have been widely used since their introduction from Raissi et al. (2019) to approximates solution of Partial Differential Equation (PDE) via NNs. However, in this paper, representing solution of Ordinary Differential Equation (ODE) is sufficient. Moreover, PINNs approximates this solution with NNs and it can be written as

$$\phi_t + \mathcal{N}[\phi] \approx f_t + \mathcal{N}[f] = 0, \quad t \in [0, t_{ub}]$$
(4)

where f represents the solution of the ODE and $\mathcal{N}[\cdot]$ is the nonlinear differential operator. ϕ is the output of PINNs and it depends on the input data and the weight of the networks (θ) . The solution f and ϕ is only valid for the bounded states and time. Additionally, the subscript -, represents the derivative with respect to time. ϕ_t can be evaluated by applying chain rule during the training with automatic differentiation. Here, the left-hand-side of Eq. (4) is defined as F

$$F := \phi_t + \mathcal{N}[\phi] \approx 0 \tag{5}$$

where F is approximately zero since ϕ is only an approximation of the f. Therefore, a restriction on the loss function can be imposed to satisfy this condition. For the training of the network, three datasets are required, which are the initial conditions dataset, the measurement dataset, and the collocation point dataset. The measurement dataset is defined as follows

$$D_{meas} = \left\{ \left(d_i^{meas}, x_{k+1,i}^{meas} \right) \right\}_{i=1}^{n_{meas}},$$

$$d_i^{meas} = \tau_i^{meas}, x_{k,i}^{meas}, u_{k,i}^{meas}, w_{k,i}^{meas}, i = 1, \dots, n_{meas}$$

$$(6)$$

where the number of measurement datapoints is denoted by n_{meas} and it is a positive constant number, d_i^{meas} is the i-th input datapoint consisted of states $(x_{k,i})$, control $(u_{k,i})$, wave height $(w_{k,i})$, and their corresponding solution $(x_{k+1,i})$ with arbitrary timestep (τ_i) . This dataset can be taken from the results of the experiment, but in this paper, it is assumed that the dataset is the solution of a discrete system. The next dataset, initial condition dataset, does not require knowledge of the model and restricts the network to output the same states when timestep is zero.

$$D_{init} = \left\{ \left(d_i^{init}, x_{k+1,i}^{init} \right) \right\}_{i=1}^{n_{init}},$$

$$d_i^{init} = \tau^{init}, x_{k,i}^{init}, u_{k,i}^{init}, w_{k,i}^{init}, \quad \tau^{init} = 0,$$

$$x_{k+1,i}^{init} = x_{k,i}^{init}, \quad i = 1, \dots, n_{init}$$
(7)

with n_{init} as the number of initial condition datapoints, and it is a positive constant number. The last dataset is the collocation point dataset which will be utilised to evaluate Eq. (5) in the loss function. The dataset is as described below

$$\mathcal{D}_{col} = \left\{ d_i^{col} \right\}_{i=1}^{n_{col}}, d_i^{col} = \left(\tau_i^{col}, x_{k,i}^{col}, u_{k,i}^{col}, w_{k,i}^{col} \right), \tag{8}$$

where n_{col} as the number of collocation datapoints, and it is a positive constant number. Based on these datasets, the loss function for the PINNs is defined as follows

$$\mathcal{L}_{total} = \alpha_1 \mathcal{L}_{meas} + \alpha_2 \mathcal{L}_{init} + \alpha_3 \mathcal{L}_{phys}$$
(9a)

$$\mathcal{L}_{init} = \frac{1}{n_{init}} \sum_{i=1}^{n_{init}} |\phi(d_i^{init}) - x_{k+1,i}^{init}|^2$$
(9b)

$$\mathcal{L}_{meas} = \frac{1}{n_{meas}} \sum_{i=1}^{n_{meas}} |\phi(d_i^{meas}) - x_{k+1,i}^{meas}|^2$$
 (9c)

$$\mathcal{L}_{phys} = \frac{1}{n_{col}} \sum_{i=1}^{n_{col}} |F(d_i^{col})|^2$$
(9d)

where \mathcal{L}_{total} , \mathcal{L}_{meas} , \mathcal{L}_{init} , \mathcal{L}_{phys} are the total losses, loss due to measurement, initial condition, and collocation point dataset respectively; α_1 , α_2 , α_3 are the weights for each loss components. In conventional NNs, the loss function typically consists of only initial condition and measurement losses. In contrast, collocation point dataset contribute to the total loss function in PINNs. This additional loss term is evaluated with only a prior physical model, eliminating the need for additional measurement from the system. Therefore, PINNs demonstrate better sample efficiency than traditional NNs, since they can, in the extreme case, be trained by only using the collocation point dataset. Nevertheless, when the knowledge of the model from Eq. (5) is not very accurate, the weights of the loss function can be tuned to be larger in the measurement and initial condition dataset.

Remark 4. To evaluate the physics loss, there are two terms to be considered: 1) To calculate nonlinear differential operator $\mathcal{N}[\cdot]$, the known model is utilised. 2) To evaluate the partial derivative with respect to time of the output of the PINNs (ϕ_t) , the automatic differentiation is utilised. At the beginning of training, the physics loss is typically large, as the NNs have not yet adapted to satisfy the governing equation. As training progresses, the physics loss tends to decrease as the network learns to approximate the solution that aligns with the governing dynamics.

In addition to the three datasets, validation dataset is produced to test the accuracy of the model as well as comparing the trained model with different hyperparameters. This dataset is similar to the measurement dataset in Eq. (6) and can be defined as follows.

$$\begin{split} \mathcal{D}_{val} &= \left\{ \left(d_i^{val}, x_{k+1,i}^{val} \right) \right\}_{i=1}^{n_{val}}, \\ d_i^{val} &= \tau_i^{val}, x_{k,i}^{val}, u_{k,i}^{val}, w_{k,i}^{val}, \quad i = 1, \dots, n_{val} \end{split} \tag{10}$$

where n_{val} is the number of validation datapoints, and it is a positive constant number. The metric to evaluate the model is Mean Squared Error (MSE) below.

$$MSE_{accuracy} = \frac{1}{n_{val}} \sum_{i=1}^{n_{val}} |\phi(d_i^{val}) - x_{k+1,i}^{val}|^2,$$

$$i = 1, ..., n_{val}$$
(11)

3.2. Implementation of PINNs-MPC

In this section, the implementation of PINNs training, the PINNs for self-loop prediction, and the PINNs-MPC will be explained. Fig. 1 outlines the structure of PINNs and the training process is explained in Algorithm 1. PINNs is structured as a fully-connected NNs consisting of input layer, normalisation layer, hidden layer with weight (θ) , and output layer. The input layer includes features such as wave prediction, timestep, system states, and control inputs, which are normalised according to their respective upper and lower bounds. These normalised inputs are then passed through the hidden layers to predict the output, which represents the next system states. The derivative of the output with respect to the timestep is computed to evaluate the physics-based loss, as defined in Eq. (9d). The total loss is then calculated, and the network weights are updated using a gradient descent algorithm, L-BFGS (Nocedal, 1980).

In Section 3.1, it is explained that the prediction for the next states (x_{k+1}) in PINNs is only valid for a bounded time $(t \in [0, t_{ub}])$. However, the optimisation problem in Eq. (1) requires N-1 intermediate prediction with sampling time, T_s . Therefore, the prediction is chained in autoregressive way similar in Antonelo et al. (2024), Arnold and King (2021), and Nicodemus et al. (2022). This method is illustrated

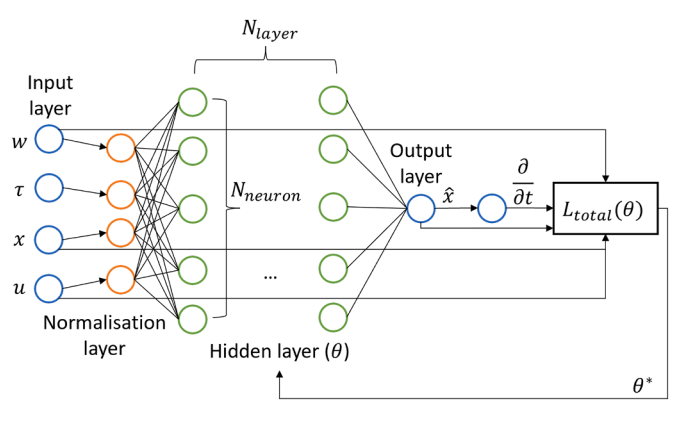


Fig. 1. PINNs training.

Algorithm 1 PINNs model training.

- 1: **Initialisation:** Generate training data (\mathcal{D}_{meas} , \mathcal{D}_{init} , \mathcal{D}_{col} , \mathcal{D}_{val}), specify training epoch (N_{epoch}), learning rate, number of layers and neurons, initialise weights (θ)
- 2: Initialise training:
- 3: **for** i **from** 0 **to** training epoch N_{epoch} , **do**
- 4: Calculate the loss function in Eq. (9a) using the current weight, θ
- 5: Calculate gradient of loss function in Eq. (9a) w.r.t. weight $(\frac{\partial \mathcal{L}_{total}}{\partial \theta})$
- Using L-BFGS algorithm, update the weight using the obtained gradient
- 7: end for
- 8: Model evaluation: using Eq. (11), evaluate the MSE of the model

in Fig. 2(a) where the timestep τ inside the PINNs is kept as T_s during the self-loop prediction and the control input (u_k) is specified by the MPC. In the self-loop process of PINNs, each new prediction (x_{k+1}) is fed back as the current state (x_k) for the next iteration. This process continues until the final prediction at N-1-th iteration is completed.

Fig. 2(b) indicates the closed-loop approach of combining PINNs and MPC. PINNs acts as the dynamic model, running in a self-loop while the MPC searches for the optimal control solution. When the MPC finds the optimal control, it is applied to the system, and the resulting system measurement is used to update the PINNs with the current state. The detailed approach is described in Algorithm 2.

Algorithm 2 PINNs-MPC scheme.

- 1: **Initialisation:** initial condition (x_0) , weights (Q, r), states and control constraints (\mathbb{X}, \mathbb{U}) , horizon length (N), simulation step (N_s)
- 2: Initialise MPC:
- 3: for i from 0 to simulation horizon (N_s) , do
- 4: Solve optimisation problem in Eq. (1) with PINNs running in self-loop as the dynamic model
- 5: Apply the first optimal control input to the system
- 6: Measure the next states (x_{k+1}) and set it as the current state (x_k)
- 7: end for

4. Simulation of point absorber with realistic wave data

This section presents the simulation results across two case studies: linear and nonlinear WECs with viscous damping. The point absorber is chosen as the case study since this configuration is a benchmark (Genest and Ringwood, 2016; Hals et al., 2011; Cretel et al., 2010; Kracht et al., 2015; Anderlini et al., 2016; Richter et al., 2013; Jia et al., 2021; Gu et al., 2021; Zhang and Li, 2020; Zhan and Li, 2019). Given the novelty

of the proposed method, this study begins with a well-established benchmark model. Extending the approach to other WEC configurations is achievable, and in some cases, straightforward, requiring only to retrain the PINNs. Section 4.1 outlines the training parameters and hyperparameter tuning of the PINNs. Section 4.2 compares open-loop performance of PINNs and conventional NNs, including an analysis of sampling efficiency. Section 4.3 evaluates closed-loop performance and energy capture of PINNs-MPC, NNs-MPC, and MPC controllers using a linear WECs model. Section 4.4 analyses the energy generation performance of the proposed method under different wave conditions. Section 4.5 compares the closed-loop performance using nonlinear WECs model with viscous damping.

A floating point absorber (Fig. 3) is considered in both case studies. The device is fixed at the seabed and constrained to only move in the heave direction. A hydraulic PTO system is installed in the cylinder below the float to extract energy from the heave movement. An example of the realisation of this design can be found in Weiss et al. (2012). The mid-point of the float and the seawater level are represented by z_v and z_w respectively. Although the model of the device is linear, it is a benchmark problem in WECs control problem. As the structure of the WECs becomes more complicated, i.e. nonlinear model and soft body WECs (Boren, 2021), PINNs can be extended to make a contribution in these areas.

With Newton's second law in the heave direction, the dynamic equation can be written as follows

$$m_{s}\ddot{z}_{v} = -f_{s} - f_{r} + f_{e} + f_{u} \tag{12}$$

where m_s is the mass of the float. The forces acting on the float are the hydrostatic restoring force (f_s) , radiation damping force (f_r) , wave excitation force (f_e) , and piston force (f_u) . Similar to Zhang et al. (2020b), Zhan and Li (2019) and Yu and Falnes (1995), Eq. (12) can be transformed into a tenth-order continuous-time state space representation.

$$\begin{cases} \dot{x} = A_c x + B_{u,c} u + B_{w,c} w + \epsilon \\ y = C_c x \end{cases}$$
 (13)

with

$$A_{c} = \begin{bmatrix} 0 & 1 & 0_{1 \times n_{r}} & 0_{1 \times n_{e}} \\ -\frac{k_{s}}{m} & 0 & -\frac{C_{r}}{m} & \frac{C_{e}}{m} \\ 0_{n_{r} \times 1} & B_{r} & A_{r} & 0_{n_{r} \times n_{e}} \\ 0_{n_{e} \times 1} & 0_{n_{e} \times 1} & 0_{n_{e} \times n_{r}} & A_{e} \end{bmatrix}, B_{u,c} = \begin{bmatrix} 0 \\ \frac{1}{m} \\ 0_{n_{r} \times 1} \\ 0_{n_{e} \times 1} \end{bmatrix},$$

$$B_{w,c} = \begin{bmatrix} 0 \\ 0 \\ 0 \\ 0_{n_{r} \times 1} \\ B_{e} \end{bmatrix}, C_{c} = \begin{bmatrix} 0 & 1 & 0_{1 \times (n_{r} + n_{e})} \end{bmatrix}$$

$$(14)$$

where $\boldsymbol{w} = \boldsymbol{z}_w$ is the wave elevation that is assumed to be predictable, $m = m_s + m_{\infty}$, m_{∞} is the infinite frequency added mass of the float, $k_s = \rho g S$ is the hydrostatic stiffness, ρ is the water density, g is the gravitational acceleration, and S is the cross-sectional area of the float. Since the float is cylindrical, S is simply the area of a circle. $(A_r, B_r, C_r, 0), x_r$ n_r are the state space representation, the states, and the number of states of the radiation force. $(A_{\rho}, B_{\rho}, C_{\rho}, 0), x_{\rho}, n_{\rho}$ are the state space representation, the states, and the number of states of the excitation force. These state space representations can be obtained via hydrodynamic software such as WAMIT (Lee, 1995) or NEMOH (Kurnia and Ducrozet, 2023). Here, ϵ represents modeling uncertainty due to the inaccurate wave prediction or linear model assumption. The notation (0) without a subscript represents the scalar zero, while the zero with subscript denotes a zero matrix whose dimensions are indicated by the subscript. $y = \dot{z}_v$ is the output, $x = [z_v, \dot{z}_v, x_r, x_e]^T$ are the states, and $u = f_u$ is the control input. To simplify the notation, the notation, v, will be dropped, and the first two states will be referred as z and \dot{z} .

The continuous-time model in Eq. (13) can be converted to a discrete-time model with Euler's discretisation or Zero Order Hold

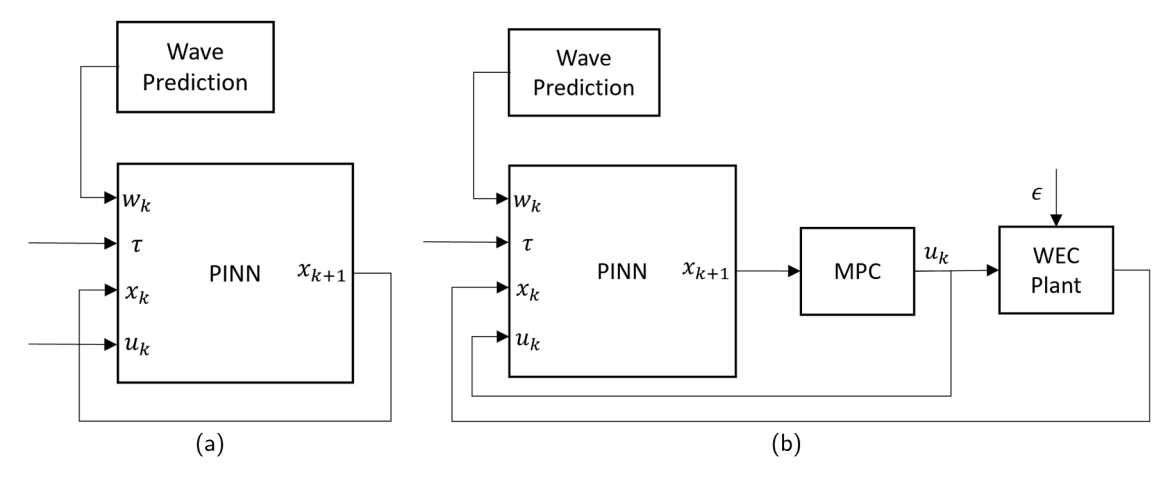


Fig. 2. PINNs prediction method. (a) self-loop. (b) closed-loop with MPC.

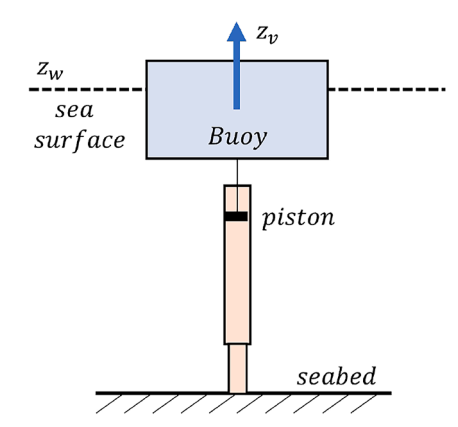


Fig. 3. Schematic diagram of floating point absorber type of WECs.

(ZOH).

$$\begin{cases} x_{k+1} = A_d x_k + B_{u,d} u_k + B_{w,d} w_k + \epsilon_k \\ y_k = C_d x_k \end{cases}$$
 (15)

where $(A_d, B_{u,d}, B_{w,d}, C_d)$ are the discrete-time version of the continuous-time matrices $(A_c, B_{u,c}, B_{w,c}, C_c)$.

The second model that is considered in this paper is nonlinear model with nonlinear viscous drag force, f_{nl} , defined as follows:

$$f_{nl} = -k_{nl}|\dot{z}|\dot{z} \tag{16}$$

where $k_{nl} = 0.5 \rho C_d S_d$ with characteristic area (A_d) and drag coefficient (C_d) that are determined by the method presented in Giorgi and Ringwood (2017). By including this nonlinear term, the state-space model in Eq. (13) is modified as:

$$\begin{cases} \dot{x} = A_c x + B_{u,c} \left(u - k_{nl} |\dot{z}| \dot{z} \right) + B_{w,c} w + \epsilon \\ y = C_c x \end{cases}$$
 (17)

A similar formulation of Eq. (17) can be found in O'Sullivan et al. (2018), Karthikeyan et al. (2019), and Zhan et al. (2025). The inclusion of a state-space form in this paper is motivated by the need for direct comparison with conventional model-based MPC approaches in subsequent simulations. PINNs can be trained without the explicit formulation of the system in state-space form, even when the governing dynamics are expressed in PDE/ODE form.

4.1. Training parameters

In this section, the training parameters for the PINNs are explored. The network architecture of the PINNs is based on a fully connected

feedforward neural network. This choice is motivated by the need for a simple and differentiable structure that facilitates smooth gradient propagation. This is important for enforcing the physics-based loss through automatic differentiation. Despite its simplicity, this architecture is effective, as the incorporation of physics-informed loss functions provides additional bias that guides the model toward physically consistent predictions. Consequently, the network can achieve improved generalisation and accuracy, even with limited measurement data.

To build the PINNs, Tensorflow in Python is utilised. and the hyperparameters are learning rate, number of layers and neurons, epoch, activation functions, and number of datapoints for each dataset. Only the first two hyperparameters are investigated to simplify the tuning process. The chosen activation function is tanh since it is smooth and differentiable, which is essential for computing accurate derivatives required in enforcing physics constraints. Moreover, tanh outputs bounded values, which helps stabilise training and improves convergence. The weights of the networks are initialised by Xavier's initialisation, and the weights on the loss function in Eq. (9a) are set as $\alpha_1 = \alpha_2 = \alpha_3 = 1$. CPU is used for training with the specification of 24-cores Intel Core i9-14900K.

For the dataset, the data is sampled with Latin Hypercube Sampling (LHS) (McKay et al., 2000) with $n_{init}=100, n_{meas}=500, n_{col}=10000, n_{val}=2649$. This method provides better sampling coverage in the input space, which is important for systems with high-dimensional inputs. The bound for the data sampling is as follows: $0 \le \tau(s) \le 0.25$, $|z| \le 0.5$ m, $|\dot{z}| \le 1$ m/s, $|u| \le 6$ kN, $|w| \le 3$ m. From Nicodemus et al. (2022), it is reasonable to set the bound of timestep for training to be slightly larger than the timestep that will be used by the controller. The sampling bounds for the radiation and excitation states are set to their minimum and maximum possible values. Simulated trajectories are employed to generate the measurement dataset. In contrast, initial condition and collocation dataset are not derived from simulations. They are sampled using the LHS method to ensure a well-distributed coverage of the domain.

The parameters for the wave energy converter model are $m=m_s+m_\infty=242+83.5=325.5$ kg and $k_s=3866$ N/m. This corresponds to the 0.35 m radius and 0.63 m draught of the cylinder. Although the buoy is a small-scale model, the proposed control schemes remain applicable to systems of different scales. The dynamic model of the radiation and excitation force is given by Yu and Falnes (1995).

$$A_r = \begin{bmatrix} 0 & 0 & -17.9 \\ 1 & 0 & -17.7 \\ 0 & 1 & -4.41 \end{bmatrix}, B_r = \begin{bmatrix} 36.5 \\ 394 \\ 75.1 \end{bmatrix}, C_r = \begin{bmatrix} 0 & 0 & 1 \end{bmatrix}$$
 (18)

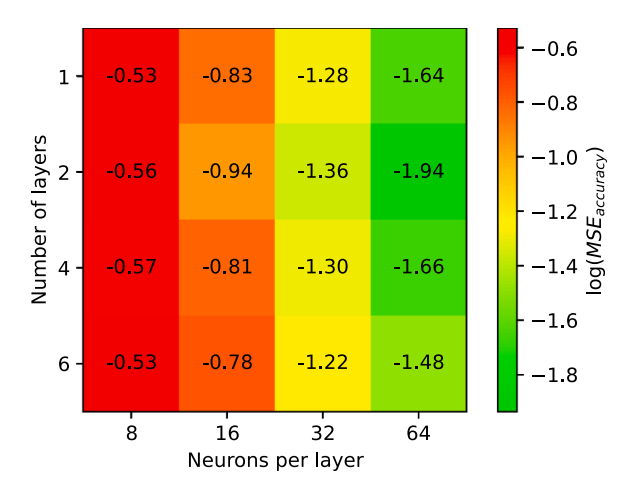


Fig. 4. Log of accuracy at the end of training of different number of layers and neurons per layer with learning rate = 0.1 (lower negative value indicate better accurary).

Table 1 Comparison of learning rates and their accuracy at the end of training (low $log(MSE_{accuracy})$ is more accurate).

Learning rate	$\log(\mathrm{MSE}_{accuracy})$
0.1	-3.74 ± 0.07
0.01	-3.33 ± 0.09
0.001	-1.74 ± 0.07
0.0001	-0.51 ± 0.07
0.00001	-0.16 ± 0.01

$$A_{e} = \begin{bmatrix} 0 & 0 & 0 & 0 & -400 \\ 1 & 0 & 0 & 0 & -459 \\ 0 & 1 & 0 & 0 & -226 \\ 0 & 0 & 1 & 0 & -64 \\ 0 & 0 & 0 & 1 & -9.96 \end{bmatrix}, B_{e} = \begin{bmatrix} 1,549,886 \\ -116380 \\ 24,748 \\ -644 \\ 19.3 \end{bmatrix}, C_{e} = \begin{bmatrix} 0 & 0 & 0 & 0 & 1 \end{bmatrix}$$
(19)

Furthermore, modelling inaccuracies are represented as random disturbances affecting the heave and its velocity state with $|\epsilon_1| \le 0.01$ and $|\epsilon_2| \le 0.1$.

To analyse the complexity of the network, a comparison between the number of layers and the number of neurons per layer is made in Fig. 4. Five different simulation seeds were used, and the resulting accuracy was averaged to produce the plot. The networks were then trained for 2000 epochs. However, for instances where convergence was not reached (neurons per layer is more than 32), the training was increased by an additional 900 epochs. It can be observed from the Figure that the most accurate network consists of 2 layers with 64 neurons per layer, requiring less computational training time than larger networks. Generally, as the number of neurons per layer increases, the accuracy improves across all layer configurations but with the cost of additional computational time.

A similar analysis was conducted for different learning rates using the network structure of 2 layers and 64 neurons, as presented in Table 1. Five different seeds were utilised, and the averaged accuracy as well as standard deviation are shown in the table. Training continued until the network converged, with varying epochs depending on the learning rate. Notably, a learning rate of 0.1 provides the best accuracy, while lower learning rates results in more training durations and low accuracy.

Based on the two previous analysis, 2 layers - 64 neurons network and a learning rate of 0.1 are chosen as the hyperparameters for the PINNs. In addition to the PINNs, two conventional NNs were trained

Table 2
The data sampling setup for the high-data NNs, low-data NNs, and PINNs.

Datapoints	PINNs	NNs High	NNs Low
n _{col}	10,000	-	-
n _{init}	100	1000	100
n_{meas}	500	100,000	500
n_{val}	2649	25,124	149

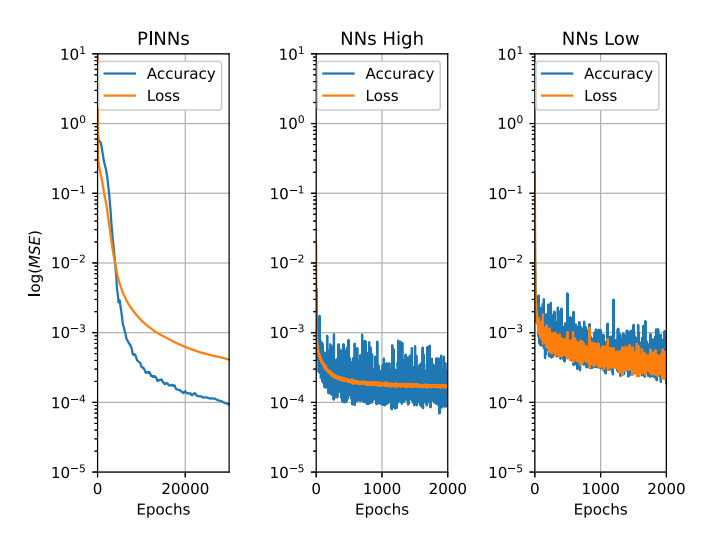


Fig. 5. Loss function and accuracy for the selected PINNs structure (2 layers, 64 neurons, learning rate = 0.1), NNs with high datapoints and low datapoints.

using hyperparameters similar to the PINNs. The key distinction lies in the training data: one NN was trained on a large dataset, while the other was trained on a significantly smaller one. This setup is intended to illustrate the sampling complexity associated with PINNs, which will be discussed in the next section. Neither of the NNs incorporates collocation points, as conventional NNs lack a mechanism to enforce physical constraints through the governing equations. The specifics of the sampling setup are specified in Table 2. The NNs are trained for 2000 epochs with ADAM (Kingma and Ba, 2015) to facilitate faster training process.

The training progress is shown in Fig. 5 by plotting both loss and accuracy over the epochs. Training the PINNs required more epochs compared to the conventional NNs, primarily due to the larger number of collocation points. For all networks, both the loss and accuracy curve rapidly decrease in the initial epochs, exhibiting a quick reduction in the model's error. They both gradually flatten, suggesting that the network has converged, and additional training epoch may not yield substantial decrease in loss or accuracy. Moreover, the parallel trends of the curves indicate that the model is effectively learning and that the training/validation datasets are well-suited to the problem. However, both curves of the PINNs appear slightly noisy. This is likely due to the discrepancy between the known physical model from the PINNs and the real model utilised by the measurement and validation datasets, which contains uncertainty. In contrast, the curves appear noticeably noisier for the NNs. This is due to the use of a different optimiser which is selected to accelerate training.

4.2. Open loop simulation

In this section, the performance of the trained PINNs is evaluated in comparison to conventional NNs. Fig. 6(a)–(b) shows the self-loop prediction with a timestep of 0.2 s. Fig. 6(a)–(b) illustrate the self-loop prediction results using a timestep of 0.2s. The prediction spans 20 steps ahead under a sinusoidal control input with zero wave height input, corresponding to the prediction horizon length typically used in a MPC framework. Comparisons are drawn among predictions generated by the

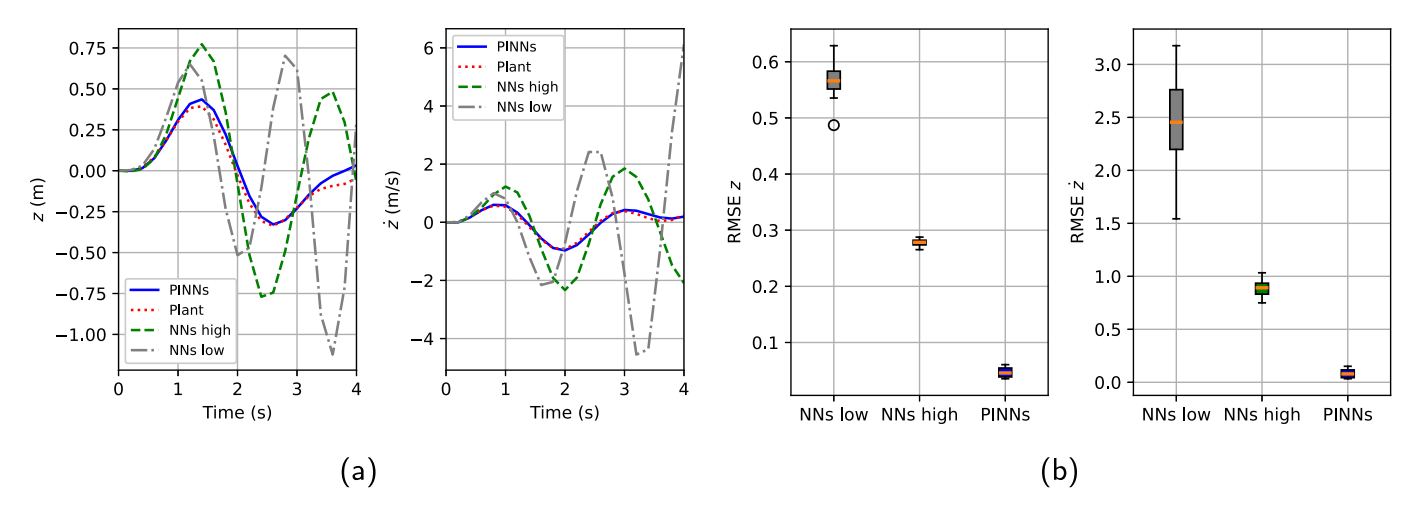


Fig. 6. Self-loop simulation of PINNs, NNs High, and NNs Low. (a) one trajectory of the heave (z) and the heave velocity (\dot{z}) . The plant is RK45 solution of Eq. (14). (b) RMSE boxplot of the heave (z) and the heave velocity (\dot{z}) for 20 trajectories.

PINNs, NNs trained on large and small datasets, and the plant solution obtained via the explicit Runge-Kutta method of order 5 (RK45) applied to Eq. (14).

In both the displacement and velocity trajectories (Fig. 6(a)), the PINNs self-loop solution initially aligns well with the exact solution. However, deviations become noticeable near the peaks and troughs of the curves after several seconds. Despite these discrepancies, the overall system dynamics are effectively captured. These results suggest that PINNs can be utilised within the MPC framework, as MPC computations primarily rely on the initial prediction rather than the accuracy of the latter half of the prediction.

In contrast, the NNs trained with fewer data points fails to accurately represent the system dynamics, despite being trained with the same number of initial and measurement datapoints ($n_{\rm init}$ and $n_{\rm meas}$) as the PINNs. This suggests that PINNs are able to utilise available data more effectively through the incorporation of collocation points, thereby achieving higher accuracy under similar data constraints. Therefore, PINNs has lower sampling complexity than of the NNs. Although the NNs trained with more datasets demonstrate improved performance relative to their low-data counterparts, they still fail to accurately capture the full system dynamics. To quantify the accuracy of the prediction, Root Mean Square Error (RMSE) is defined in Eq. (20).

$$RMSE = \sqrt{\frac{1}{n_{test}} \sum_{i=1}^{n_{test}} (\hat{X}_i - X_i)^2}$$
 (20)

where n_{test} is the number of datapoints for the RMSE calculation, \hat{X}_i is the i-th datapoint of the PINNs/NNs, and X_i is the i-th datapoint of the plant. In this section, the $n_{test}=20$ corresponding to the 20 steps ahead prediction. Fig. 6(b) presents the Root Mean Square Error (RMSE) computed over 20 simulated trajectories with respect to the plant output. For both displacement (z) and velocity (\dot{z}), the PINNs consistently yield lower RMSE compared to both NNs models. It is worth noting that the velocity prediction error for the low-data NNs model can reach up to 3 m/s, which significantly exceeds the expected dynamic range of the plant. This level of error is unsuitable for use in control applications. Although increasing the size of the training dataset improves the performance of the NNs model, the PINNs maintain higher accuracy in both heave and heave velocity case.

The impact of measurement noise on the predictive performance of PINNs is evaluated using a noise level metric. This is defined as the ratio of the standard deviation of noise-free data to that of noisy data, analogous to signal-to-noise (SNR) ratio. Noise is injected into the heave and heave velocity measurements datapoints respectively. Fig. 7 illustrate trajectory deviations compared to the plant under varying noise levels.

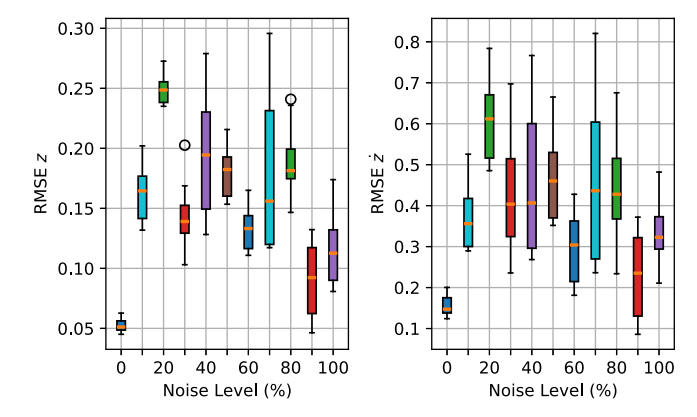


Fig. 7. RMSE of 20 trajectories of self-loop simulation of PINNs with different noise levels. RMSE is calculated compared to the plant. The trajectories have different initial conditions and control input.

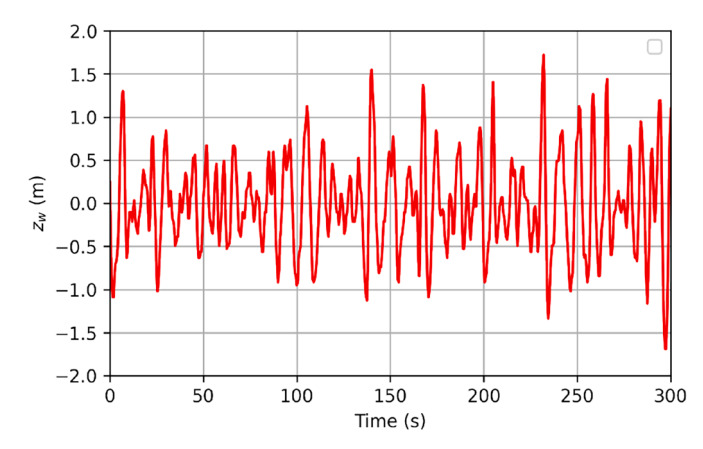
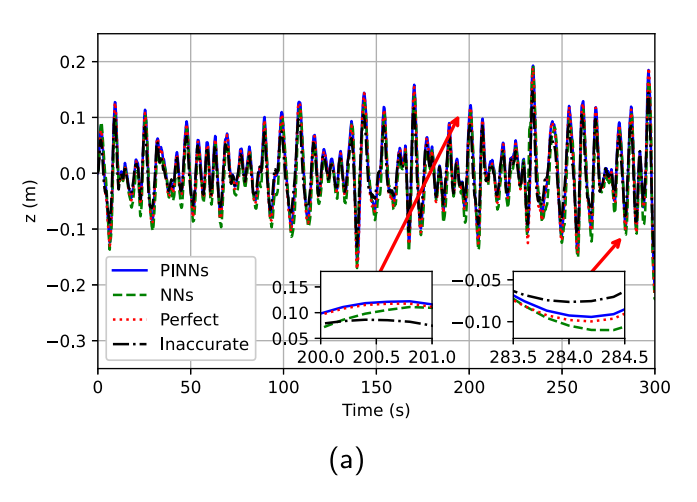


Fig. 8. Wave height data collected from the coast of Cornwall, UK. The wave data is appropriately scaled according to the size of the point absorber.

As illustrated, the RMSE for both z and \dot{z} generally increases with higher noise levels, indicating reduced prediction accuracy. This result demonstrates that, although increasing noise levels lead to higher prediction errors, the degradation in accuracy remains bounded. The RMSE values for both heave displacement and velocity do not exhibit unbounded growth or instability, even at the highest noise level tested (100 %).



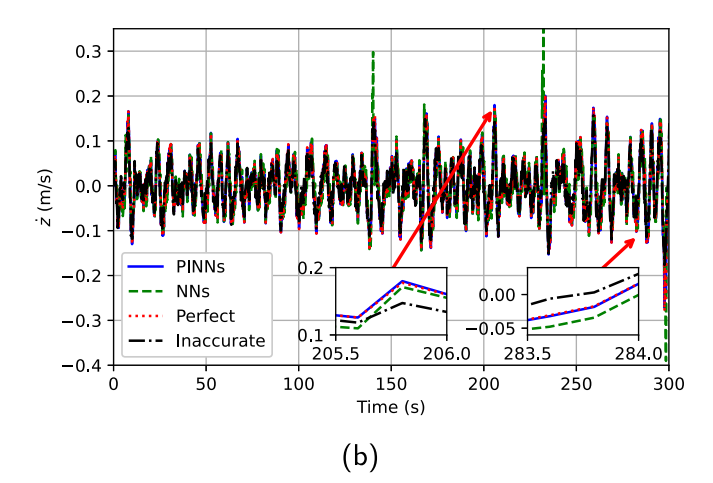


Fig. 9. Closed-loop simulation of PINNs, NNs, perfect, and inaccurate MPC. (a) \dot{z} , $|\dot{z}| \le 1$ m/s. (b) z, $|z| \le 0.5$ m.

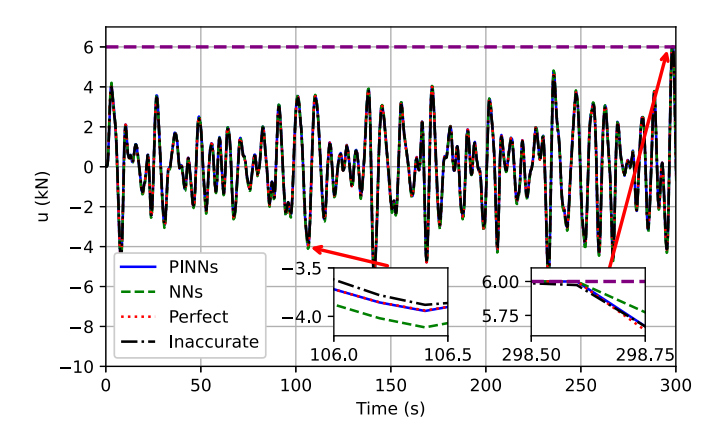


Fig. 10. Closed-loop simulation of PINNs, NNs, perfect, and inaccurate MPC for the control input, purple dotted line is the constraint ($|u| \le 6000$ N).

Table 3Model parameter of the perfect and inaccurate MPC.

Parameter	Perfect	Inaccurate
k _s	3866	3092.8
m	325.5	260.4

4.3. Closed loop simulation

In this section, the performance of the closed-loop PINNs-MPC is compared to NNs-MPC with high datapoints and MPC with perfect model and inaccurate model. The model is outlined in Table 3. The inaccurate model was designed to have: 1) The added mass of the system is 78 % of the perfect model. This corresponds to 20 % mass reduction of the total mass. 2) The hydrostatic restoring coefficient is 20 % less than the perfect model. In real-world application, this inaccurate model can happen due to extreme sea states where the device suffers from nonlinear friction and viscous force. In addition, the inaccurate model does not have perfect wave radiation force calculation. Noise with uniform distribution from -0.15 to 0.15 N is injected into the wave radiation force. This modelling choice is justified because, in practice, wave radiation forces must be estimated which are inherently imperfect and subject to noise. The NNs model that is used in this section is the NNs with high datapoints from the previous section.

The weight matrix Q is the same for all models, defined as $Q = \operatorname{diag}(7,7,0_{1\times(n_r+n_e)})$ while the weight r is 0.0001. The controller was tuned by adjusting r until the control input (u) reached the constraint. The

prediction horizon N is 15 steps, and a 300-second simulation is conducted with a 0.2-second timestep. In practice, a timestep of 0.2 seconds is sufficient to effectively control the dynamics of WECs. Faster timestep can affect the performance of the actuator since the actuator is unable to respond to rapid input changes.

The state and control input constraints are the same as the data sampling bounds described in Section 4.1. To implement MPC, the structure of the PINNs was converted from TensorFlow to CasADi (Andersson et al., 2019), enabling the use of a standard MPC solver. The do-mpc library (Fiedler et al., 2023) was implemented with IPOPT (Wächter and Biegler, 2006) as the solver. The initial conditions for the simulation were $x = [0;0;0_{1\times(n_r+n_e)}]$. In addition, the predicted wave is not perfect and within a prediction horizon, the predicted wave is

$$w_k = w_k + \epsilon_0 e^{\lambda s_k}, k = 1, 2, \dots, N, s_k = 0, T_s, \dots, (N-1)T_s$$
 (21)

where ϵ_0 is uniformly sampled from -0.2 to 0.2 and $\lambda=0.5$. This prediction is designed such that the error grows with the prediction time. The wave height used in this section is shown in Fig. 8. This is a segment of real wave data collected from the coast of Cornwall, and the height is bounded. In addition to the prediction error, random disturbances are also considered with uniformly sampled $|\epsilon_1| \leq 0.01$ and $|\epsilon_2| \leq 0.1$.

The results of the comparison are presented in Figs. 9–11. The states are shown in Fig. 9(a)–(b) for the velocity and displacement respectively. It can be observed that both are within their constraints although they are not active. In contrast, Fig. 10 shows that the control input constraints are active across all cases, ensuring a fair comparison.

To evaluate the performance of energy generation, the power and energy generated by the controllers are assessed, as shown in Fig. 11. After a 300-second simulation, the energy generated is 29.97 kJ for the PINNs model, 28.39 kJ for the NNs model, 30.55 kJ for the accurate model, and 23.74 kJ for the inaccurate model. This indicates that the PINNs model generates 1.9% less energy than the accurate model but still performs better than the inaccurate model and the NNs model, which results in a 22.3% and $7.06\,\%$ energy loss respectively.

To investigate the sensitivity of the tuning parameters of the MPC, comparison is made for different q_1 , q_2 , r, N with $Q=\mathrm{diag}(q_1,q_2,0_{1\times(n_r+n_e)})$ while keeping the other parameters constant. These comparisons are made for the perfect MPC. Fig. 12(a)–(c) presents the effect of tuning the MPC weighting parameters on the energy generation of the WEC system for 300 s simulation time. Lowering q_1 and q_2 results in an increase in harvested energy. By assigning smaller penalties to these states, the controller permits larger physical motion, which is beneficial for wave energy conversion since energy is extracted from the relative movement induced by waves. This is assuming that they remain well within their operational constraints. However, these weights cannot be reduced arbitrarily. If the setting is too low or to zero, the cost

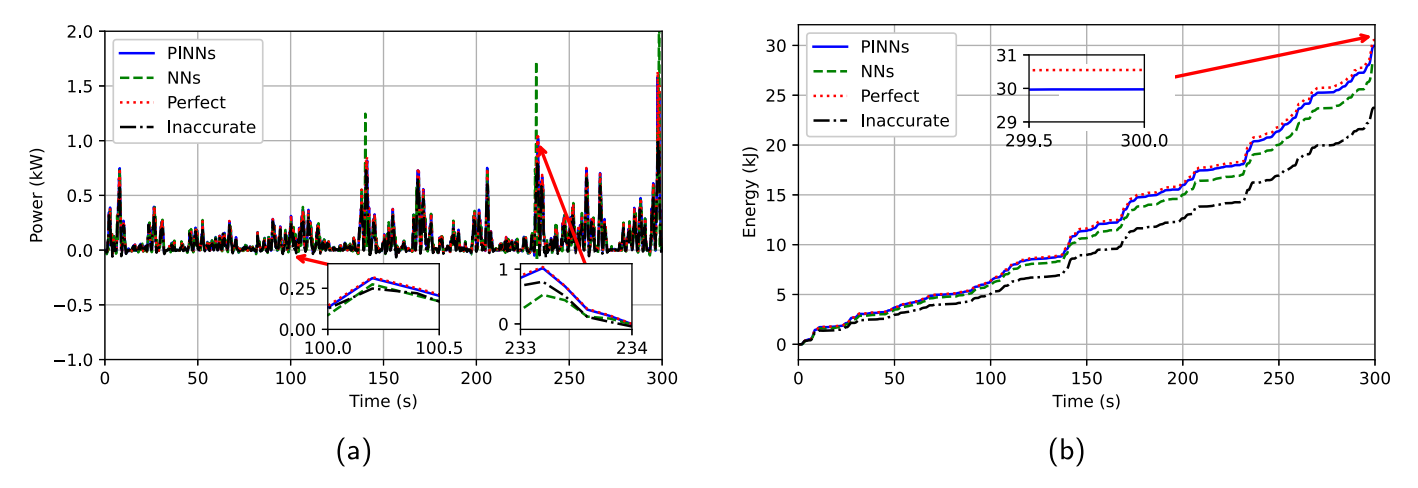


Fig. 11. Closed-loop simulation of PINNs, NNs, perfect, and inaccurate MPC. (a) Power. (b) Energy.

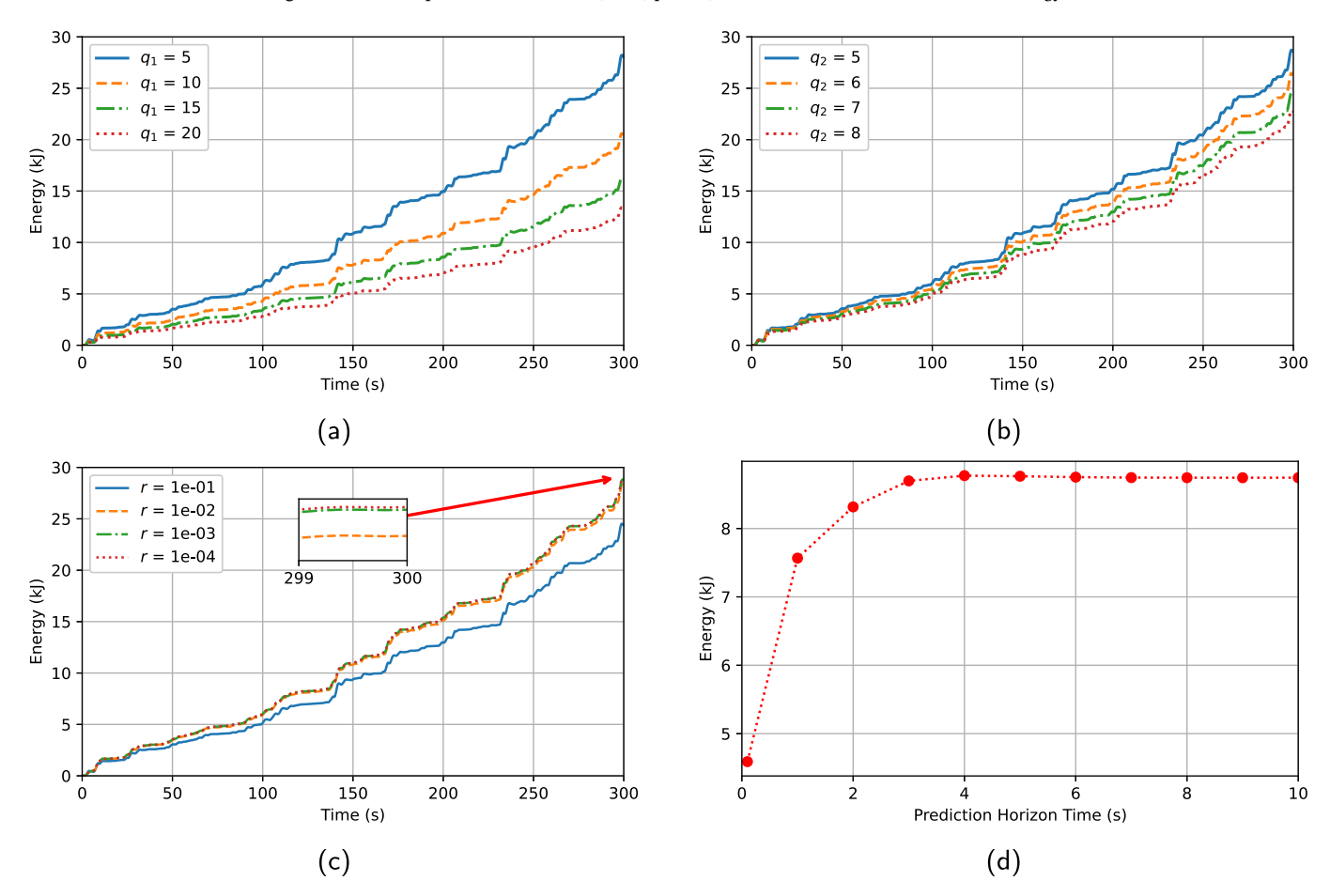


Fig. 12. Closed-loop simulation of the energy generation of perfect MPC with different tuning parameters. (a) q_1 . (b) q_2 . (c) r. (d) prediction horizon time.

function may lose its positive definiteness, leading to an infeasible optimisation problem. Therefore, a balance must be maintained to ensure both performance and numerical stability.

In comparison, reducing the control penalty r has a less pronounced effect on energy output. Although a smaller r encourages more aggressive control, the actuator is already operating near its saturation limits. As a result, a further reduction in r does not significantly increase the control input or the energy capture. This indicates that while the adjustment r contributes to the performance, it has less influence on the energy generation compared to that of the state weights when the actuator constraints are active. Another MPC tuning parameter is the prediction

horizon time, defined as $N*T_s$ in Fig. 12(d). Simulation conducted for 100 s indicates that extending the horizon improves energy generation up to 3 s. Beyond this time, increasing the prediction horizon time does not lead to increase of energy, while the computational cost will rise.

The simulations in the current section have validated the capability of PINNs-MPC to handle constraints effectively and achieve similar energy conversion efficiency to the accurate MPC model despite the presence of uncertainty. However, a limitation of this study is that the current model does not account for energy conversion beyond the PTO stage. To deliver power to the grid, it must pass through conditioning circuits to prevent grid instability due to power fluctuations. This

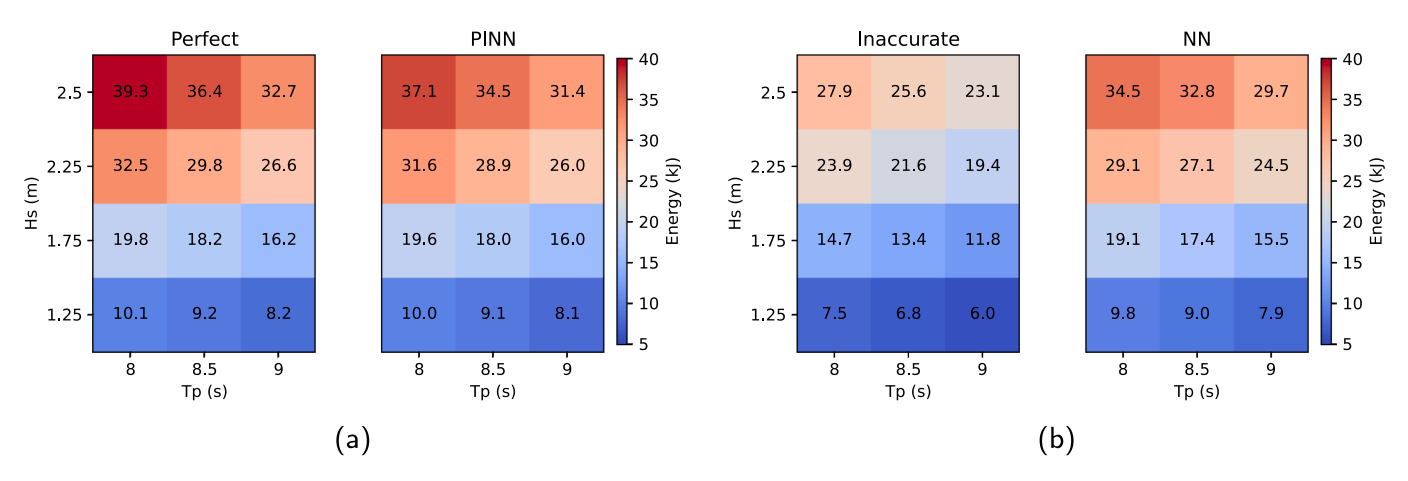


Fig. 13. Energy plot of PINNs, NNs, perfect, and inaccurate MPC of different wave conditions. (a) Perfect model and PINNs. (b) Inaccurate model and NNs.

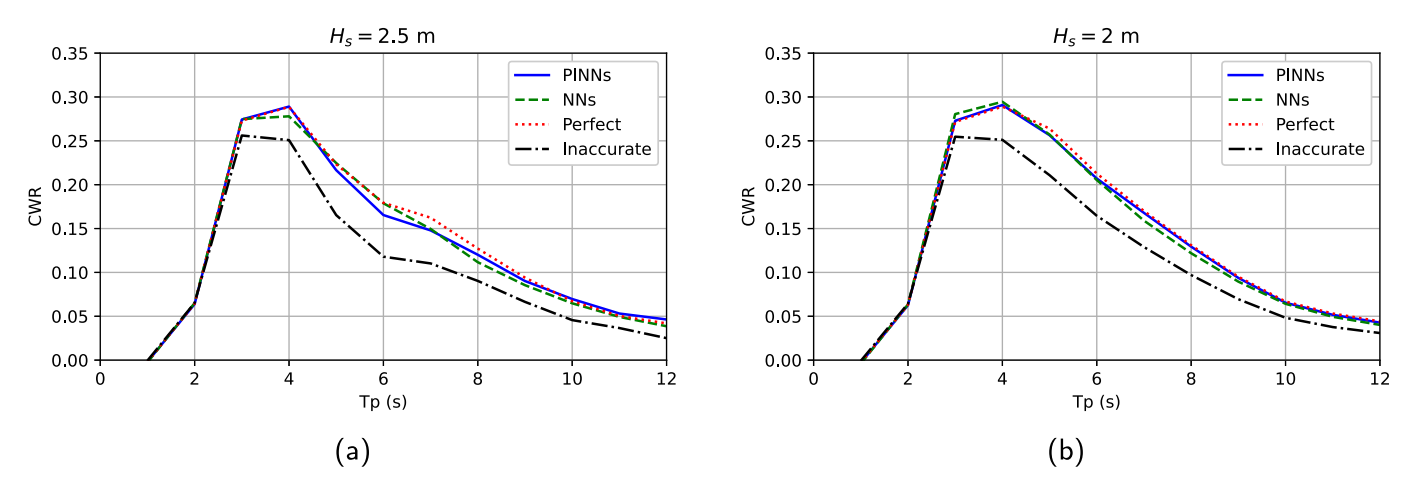


Fig. 14. CWR plot of PINNs, NNs, perfect, and inaccurate MPC of different wave conditions. (a) $H_3 = 2.5$ m. (b) $H_3 = 2$ m.

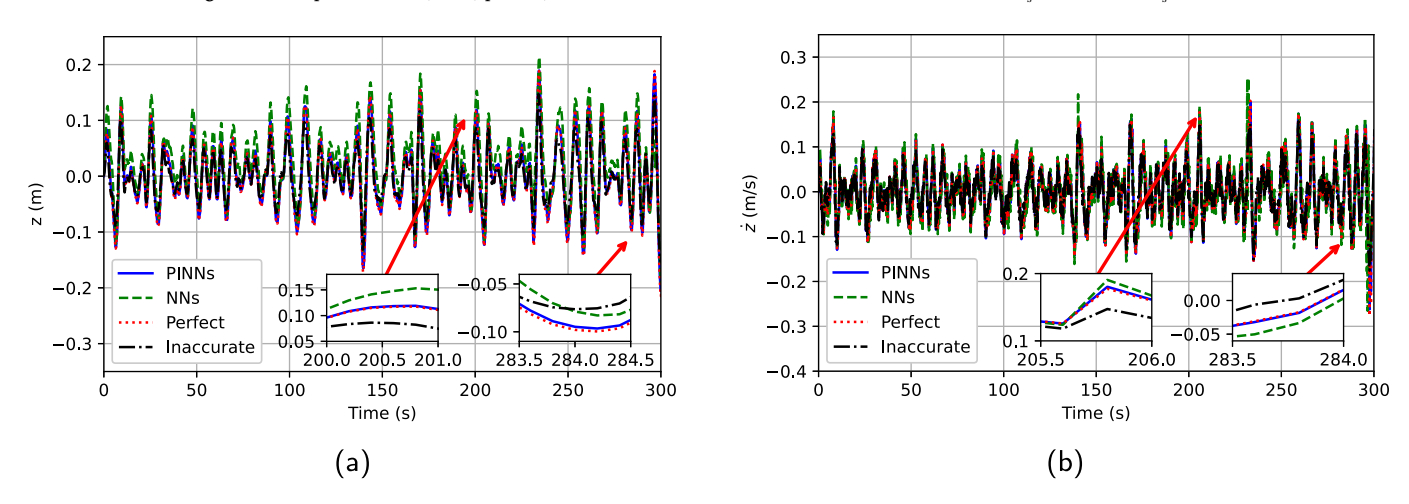


Fig. 15. Closed-loop simulation of PINNs, NNs, perfect, and inaccurate MPC with nonlinear viscous force. (a) \dot{z} , $|\dot{z}| \leq 1$ m/s. (b) z, $|z| \leq 0.5$ m.

introduces additional effects that would be interesting to explore in future work with the proposed control scheme.

4.4. Closed loop simulation with various wave conditions

This section presents a comparison of energy generation of the previously discussed methods under different wave conditions. The wave is generated by JONSWAP spectrum with a peakedness factor of 3.3. The significant wave height (H_s) ranges from 1.25 m to 2.5 m, and the peak period (T_p) spans 8 to 9 s. These conditions were selected to correspond

to Sea State 4, consistent with the wave profile used in the previous section in Fig. 8.

The result is illustrated in Fig. 13(a)–(b). The maximum energy is generated by $H_s=2.5$ m and $T_p=8$ s. The trend also shows that the higher the significant wave height, the more energy is harvested. This is consistent with the theory, since larger wave heights possess more wave energy. In contrast, the increase of the peak period leads to a decrease in the harvested energy in the simulated range. The perfect MPC performs the best under all conditions followed by PINNs-MPC, NNs-MPC, and Inaccurate MPC. Nonetheless, the PINNs-MPC controller

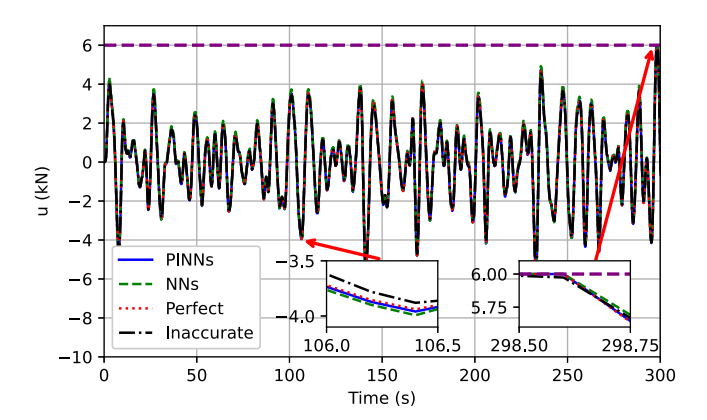


Fig. 16. Closed-loop simulation of PINNs, NNs, perfect, and inaccurate MPC for the control input with nonlinear viscous force, purple dotted line is the constraint ($|u| \le 6000$ N).

demonstrates energy capture performance that closely approaches the perfect model. For example, at $H_s=2.5~{\rm m}$ and $T_p=8~{\rm s}$, the PINNs-MPC yields 37.1 kJ, only a 5.6 % deviation from the ideal perfect MPC. At lower wave heights such as $H_s=1.25~{\rm m}$, the PINNs-MPC and perfect MPC exhibit nearly identical performance. In contrast, the inaccurate model shows degraded performance. The energy captured by this model is up to 29 % lower than that of the Perfect model under high wave conditions ($H_s=2.5~{\rm m}$ and $T_p=8~{\rm s}$), indicating that physical modelling fidelity remains critical for energy generation. The conventional NNs model performs moderately well, achieving better results than the inaccurate model but consistently underperforming relative to the PINNs-MPC. These results highlight the advantage of PINNs in terms of energy generation performance across a range of wave conditions.

Apart from the energy calculation, the capture width ratio (CWR) of the WECs is also calculated based on Babarit (2015). CWR is a quantification of the power performance of WECs and it is a measure of hydrodynamic efficiency. It can be defined as

$$CWR = \frac{\bar{P}}{P_{wave}D}$$
 (22)

where P_{wave} is the available wave power per unit meter, D is the characteristic length of the WECs, \bar{P} is the average mechanical power generated by the WECs. For the point absorber, the characteristic length is simply the diameter of the device, D=0.7 m. Moreover, P_{wave} is estimated based on the H_s and T_p (Guillou, 2020). The results of the CWR calculation are shown in Fig. 14(a)-(b). The significant wave height is fixed at $H_s=2.5$ m and $H_s=2$ m, and the peak period varies from 1 to 12 s with a 1 s interval. These parameter ranges are consistent with

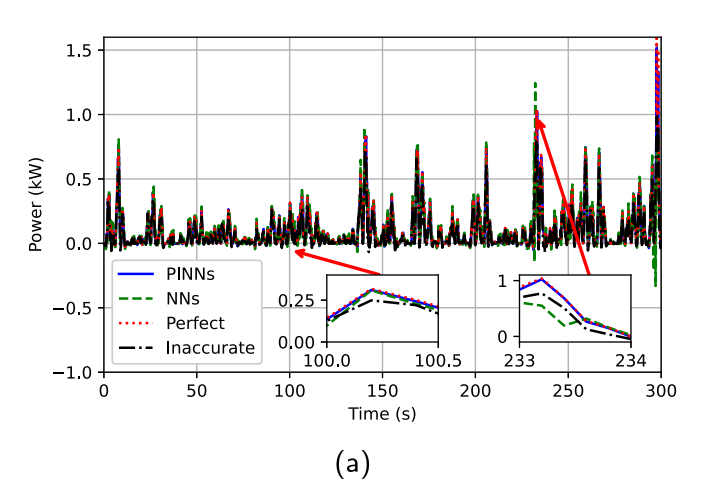
those commonly employed in previous CWR evaluation study (Carpintero Moreno and Stansby, 2019; Zhang and Li, 2020). The maximum CWR is found when the peak period is 4 s, and this is caused by the natural heave period of the device combined with the tuning from the controller. It can be observed that the PINNs-MPC closely follows the perfect MPC. At the peak period of 4 s with $H_s=2.5\,\mathrm{m}$, PINNs-MPC significantly outperforms the NNs and inaccurate MPC. These simulations demonstrate the ability of PINNs-MPC to approximate the perfect model with various wave conditions. In addition, CWR should remain nearly constants for all H_s since it is a non-dimensional parameter. However, in this study, the CWR can increase or decrease for different H_s due to the limitation of PTO.

4.5. Closed loop simulation with nonlinear WECs plant

This section presents a case study incorporating plant nonlinearity to demonstrate the performance of the proposed control scheme on energy generation. For the current device, the resulting viscous force coefficient is $k_{nl}=48\,\mathrm{kg/m}$. A similar setup is employed to retrain both the PINNs and NNs, after which the resulting models are integrated into the MPC framework. The closed-loop performance of the PINNs-MPC and NNs-MPC schemes is compared against two controllers: the perfect MPC and an inaccurate MPC, under identical settings as previously described. This comparison is illustrated in Figs. 15–17. The heave displacement and velocity responses demonstrate that the system states remain well within their respective constraints across all cases. In contrast, the control input constraint is active throughout the simulations, thereby ensuring a fair comparison among the different control strategies.

To evaluate the performance of energy generation, the energy output of each controller is assessed over a 300-second simulation period, as shown in Fig. 17. The perfect MPC yields the highest energy output at 30.53 kJ. The PINNs-MPC achieves 30.02 kJ, corresponding to an energy loss of only 1.69% relative to the perfect case. The NNs-MPC produces 29.17 kJ, resulting in a 4.46% reduction in energy. In contrast, the inaccurate model generates only 23.74 kJ, exhibiting a significantly larger energy loss of 22.25%. These results highlight the effectiveness of the proposed PINNs-MPC in capturing the system dynamics under nonlinear conditions and maintaining high energy generation performance.

Apart from the WECs control problem, PINNs-MPC framework shows strong potential for broader application in renewable energy systems such as wind and solar, which often face challenges related to modeling complexity, data sparsity, and control under constraints. In wind energy, highly nonlinear and time-varying aerodynamics, turbine wake interactions, and environmental uncertainties complicate accurate modeling. Similarly, solar power systems must cope with rapidly changing irradiance, partial shading, and battery degradation dynamics, all under



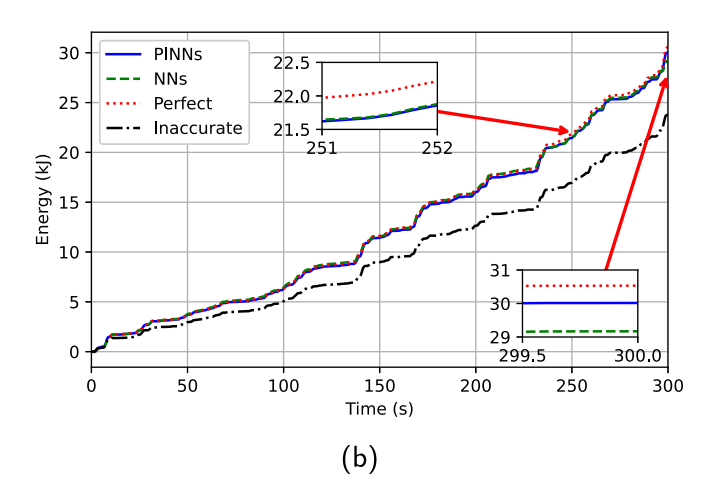


Fig. 17. Closed-loop simulation of PINNs, NNs, perfect, and inaccurate MPC with nonlinear viscous force. (a) Power. (b) Energy.

tight operational constraints. PINNs can offer a solution by incorporating partially known physical laws directly into the learning process, enabling accurate system identification from sparse measurements. When combined with MPC, this allows for constrained optimal control that is physically consistent, making it a powerful tool for improving energy generation performance and reliability in renewable energy applications.

Nonetheless, applying this control strategy to other renewable energy systems requires several adaptations. First, the partially known governing equations used in the PINNs formulation must be revised to reflect the physical principles governing the target system, followed by retraining with relevant data. Additionally, the MPC cost function should be redefined to reflect the performance objectives of the energy source, such as maximising power output in photovoltaic or wind turbine systems, while explicitly incorporating the physical and operational constraints. Despite these modifications, the proposed framework remains broadly applicable to a range of renewable energy technologies.

5. Conclusions

In conclusion, this study presented a novel application of the PINNs-MPC framework for optimising the energy output of WECs. The results from simulation studies demonstrated the sampling efficiency of PINNs compared to the traditional NNs. Moreover, the PINNs-MPC scheme achieved comparable energy conversion efficiencies to traditional MPC with perfect knowledge of system dynamics, while outperforming models with inaccurate information and the NNs MPC. Additionally, the use of PINNs models has been extensively validated through hyperparameter tuning and open-loop simulations. Future work will focus on an experimental study with the proposed PINNs-MPC scheme.

CRediT authorship contribution statement

Vincentius Versandy Wijaya: Writing – original draft, Methodology, Investigation; **Yao Zhang:** Writing – review & editing, Supervision, Methodology, Conceptualization.

Declaration of competing interest

The authors declare that they have no known competing financial interests or personal relationships that could have appeared to influence the work reported in this paper.

Acknowledgment

This work was funded by Wave Energy Scottland Direct Generation Competition, the UK Royal Society IEC-NSFC (223485), Innovate UK/Department for Transportation GREENPORTSIDE project.

References

11 (1), 1-36,

- Anderlini, E., Forehand, D. I.M., Stansell, P., Xiao, Q., Abusara, M., 2016. Control of a point absorber using reinforcement learning. IEEE Trans. Sustain. Energy 7 (4), 1681–1690.
 Andersson, J. A.E., Gillis, J., Horn, G., Rawlings, J.B., Diehl, M., 2019. CasADi a software framework for nonlinear optimization and optimal control. Math. Program. Comput.
- Antonelo, E.A., Camponogara, E., Seman, L.O., Jordanou, J.P., de Souza, E.R., Hübner, J.F., 2024. Physics-informed neural nets for control of dynamical systems. Neurocomputing 579, 127419.
- Arnold, F., King, R., 2021. State–space modeling for control based on physics-informed neural networks. Eng. Appl. Artif. Intell. 101, 104195.
- Babarit, A., 2015. A database of capture width ratio of wave energy converters. Renew. Energy 80, 610–628.
- Babarit, A., Clément, A.H., 2006. Optimal latching control of a wave energy device in regular and irregular waves. Appl. Ocean Res. 28 (2), 77–91.
- Barone, P., Truscelli, F., Castiglione, T., Bova, S., 2024. Latching control of a point-absorber wave energy converter with a hydraulic power take-off system: a calabrian case study. Ocean Eng. 310, 118775.
- Belmont, M.R., Christmas, J., Dannenberg, J., Hilmer, T., Duncan, J., Duncan, J.M., Ferrier, B., 2014. An examination of the feasibility of linear deterministic sea wave prediction in multidirectional seas using wave profiling radar: theory, simulation, and sea trials. J. Atmos. Oceanic Technol. 31 (7), 1601–1614.

- Boren, B., 2021. Distributed embedded energy converters for ocean wave energy harvesting: enabling a domain of transformative technologies. Proceedings of the European Wave and Tidal Energy Conference. National Renewable Energy Laboratory, Plymouth, United Kingdom U.S. Department of Energy, Office of Energy Efficiency and Renewable Energy.
- Budal, K., Falnes, J., 1980. Interacting point absorbers with controlled motion. Power from Sea Waves: Conference on Power from Sea Waves. Edinburgh, United Kingdom Academic Press 381–399.
- Cai, S., Wang, Z., Wang, S., Perdikaris, P., Karniadakis, G.E., 2021. Physics-informed neural networks for heat transfer problems. J. Heat Transf. 143 (6), 060801.
- Carpintero Moreno, E., Stansby, P., 2019. The 6-float wave energy converter m4: ocean basin tests giving capture width, response and energy yield for several sites. Renew. Sustain. Energy Rev. 104, 307–318.
- Cretel, J., Lewis, A.W., Lightbody, G., Thomas, G.P., 2010. An application of model predictive control to a wave energy point absorber. IFAC Proc. Vol. 43 (1), 267–272. 1st IFAC Conference on Control Methodologies and Technology for Energy Efficiency.
- EPSRC, 2020. Wave Energy Road Map. Technical Report. EPSRC.
- Erselcan, İ.Ö., Kükner, A., 2020. A parametric optimization study towards the preliminary design of point absorber type wave energy converters suitable for the turkish coasts of the black sea. Ocean Eng. 218, 108275.
- Faedo, N., Olaya, S., Ringwood, J.V., 2017. Optimal control, MPC and MPC-like algorithms for wave energy systems: an overview. IFAC Journal of Systems and Control 1, 37–56.
- Feng, Z., Kerrigan, E.C., 2013. Latching control of wave energy converters using derivative-free optimization. In: 52nd IEEE Conference on Decision and Control, pp. 7474–7479.
- Feng, Z., Kerrigan, E.C., 2015. Latchingdeclutching control of wave energy converters using derivative-free optimization. IEEE Trans. Sustain. Energy 6 (3), 773–780.
- Fiedler, F., Karg, B., Lüken, L., Brandner, D., Heinlein, M., Brabender, F., Lucia, S., 2023. Do-mpc: towards FAIR nonlinear and robust model predictive control. Contr. Eng Pract. 140, 105676.
- Frison, G., Diehl, M., 2020. Hpipm: a high-performance quadratic programming framework for model predictive control. IFAC-PapersOnLine 53 (2), 6563–6569. 21st IFAC World Congress.
- Genest, R., Ringwood, J.V., 2016. A critical comparison of model-predictive and pseudospectral control for wave energy devices. J. Ocean Eng. Marine Energy 2 (4), 485–499.
- Giorgi, G., Ringwood, J., 2017. Consistency of viscous drag identification tests for wave energy applications. In: Proceedings of the 12th European Wave and Tidal Energy Conference 27th Aug-1st Sept 2017. European Wave and Tidal Energy Conference 2017, pp. 1–8.
- Gu, Y., Ding, B., Sergiienko, N.Y., Cazzolato, B.S., 2021. Power maximising control of a heaving point absorber wave energy converter. IET Renew. Power Gener. 15 (14), 3296–3308.
- Guillou, N., 2020. Estimating wave energy flux from significant wave height and peak period. Renew. Energy 155, 1383–1393.
- Hals, J., Falnes, J., Moan, T., 2011. A comparison of selected strategies for adaptive control of wave energy converters. J. Offshore Mech. Arct. Eng. 133 (3), 031101.
- Jia, Y., Meng, K., Dong, L., Liu, T., Sun, C., Dong, Z.Y., 2021. Economic model predictive control of a point absorber wave energy converter. IEEE Trans. Sustain. Energy 12 (1), 578–586.
- Jin, S., Greaves, D., 2021. Wave energy in the UK: status review and future perspectives. Renew. Sustain. Energy Rev. 143, 110932.
- Jin, X., Cai, S., Li, H., Karniadakis, G.E., 2021. Nsfnets (navier-stokes flow nets): physics-informed neural networks for the incompressible navier-stokes equations. J. Comput. Phys. 426, 109951.
- Kaiser, M.S., Iida, T., Taniguchi, T., Katayama, T., Yoshimura, R., Irifune, K., 2025. Optimal prediction horizon length in model predictive control to maximise energy absorption by a point absorber wave energy converter. Ocean Eng. 329, 121130.
- Karthikeyan, A., Previsic, M., Scruggs, J., Chertok, A., 2019. Non-linear model predictive control of wave energy converters with realistic power take-off configurations and loss model. In: 2019 IEEE Conference on Control Technology and Applications (CCTA), pp. 270–277.
- Kingma, D.P., Ba, J., 2015. Adam: a method for stochastic optimization. In: ICLR.
- Kracht, P., Perez-Becker, S., Richard, J.-B., Fischer, B., 2015. Performance improvement of a point absorber wave energy converter by application of an observer-based control: results from wave tank testing. IEEE Trans. Ind. Appl. 51 (4), 3426–3434.
- Kurnia, R., Ducrozet, G., 2023. Nemoh: open-source boundary element solver for computation of first- and second-order hydrodynamic loads in the frequency domain. Comput. Phys. Commun. 292, 108885.
- Lee, C.H., 1995. Wamit Theory Manual, Department of Ocean Engineering.
- Liao, Z., Sun, T., Al-Ani, M., Jordan, L.-B., Li, G., Wang, Z., Belmont, M., Edwards, C., 2023. Modelling and control tank testing validation for attenuator type wave energy converter - part i: experiment setup and control-oriented modelling. IEEE Trans. Sustain. Energy 14 (3), 1747–1757.
- Lin, Z., Huang, X., Xiao, X., 2023. Fast model predictive control system for wave energy converters with wave tank tests. IEEE Trans. Ind. Electron. 70 (7), 6887–6897.
- Liu, C., Hu, M., Zhao, Z., Zeng, Y., Gao, W., Chen, J., Yan, H., Zhang, J., Yang, Q., Bao, G., Chen, S., Wei, D., Min, S., 2021. Latching control of a raft-type wave energy converter with a hydraulic power take-off system. Ocean Eng. 236, 109512.
- Liu, T., Zhao, J., Huang, J., Li, Z., Xu, L., Zhao, B., 2024. Research on model predictive control of autonomous underwater vehicle based on physics informed neural network modeling. Ocean Eng. 304, 117844.
- McKay, M.D., Beckman, R.J., Conover, W.J., 2000. A comparison of three methods for selecting values of input variables in the analysis of output from a computer code. Technometrics 42 (1), 55–61.

- Meng, Z.-F., Chen, Z., Khoo, B.C., Zhang, A.-M., 2022. Long-time prediction of sea wave trains by LSTM machine learning method. Ocean Eng. 262, 112213.
- Nicodemus, J., Kneifl, J., Fehr, J., Unger, B., 2022. Physics-informed neural networks-based model predictive control for multi-link manipulators. IFAC-PapersOnLine 55 (20), 331–336. 10th Vienna International Conference on Mathematical Modelling MATHMOD 2022.
- Nocedal, J., 1980. Updating quasi-newton matrices with limited storage. Math. Comput. 35 (151), 773–782.
- O'Sullivan, A. C.M., Sheng, W., Lightbody, G., 2018. An analysis of the potential benefits of centralised predictive control for optimal electrical power generation from wave energy arrays. IEEE Trans. Sustain. Energy 9 (4), 1761–1771.
- Pasta, E., Carapellese, F., Mattiazzo, G., 2021. Deep neural network trained to mimic non-linear economic model predictive control: an application to a pendulum wave energy converter. In: 2021 IEEE Conference on Control Technology and Applications (CCTA), pp. 295–300.
- Raissi, M., Perdikaris, P., Karniadakis, G.E., 2019. Physics-informed neural networks: a deep learning framework for solving forward and inverse problems involving nonlinear partial differential equations. J. Comput. Phys. 378, 686–707.
- Rathore, P., Lei, W., Frangella, Z., Lu, L., Udell, M., 2024. Challenges in training PINNs: a loss landscape perspective. In: Proceedings of the 41st International Conference on Machine Learning. PMLR, pp. 42159–42191.
- Richter, M., Magana, M.E., Sawodny, O., Brekken, T. K.A., 2013. Nonlinear model predictive control of a point absorber wave energy converter. IEEE Trans. Sustain. Energy 4 (1), 118–126.
- Ringwood, J.V., Bacelli, G., Fusco, F., 2014. Energy-maximizing control of wave-energy converters: the development of control system technology to optimize their operation. IEEE Contr. Syst. Mag. 34 (5), 30–55.
- Rosati, M., Henriques, J.C.C., Ringwood, J.V., 2022. Oscillating-water-column wave energy converters: a critical review of numerical modelling and control. Energy Conver. Manag. X 16, 100322.
- Shi, S., Patton, R.J., Liu, Y., 2018. Short-term wave forecasting using gaussian process for optimal control of wave energy converters. IFAC-PapersOnLine 51 (29), 44–49. 11th IFAC Conference on Control Applications in Marine Systems, Robotics, and Vehicles CAMS 2018.
- Smart, G., Noonan, M., 2018. Tidal Stream and Wave Energy Cost Reduction and Industrial Benefit. Technical Report. Offshore Renewabel Energy Catapult: Glasgow, UK.
- Systems, O.E., 2023. Ocean Energy and Net Zero: An International Roadmap to Develop 300GW of Ocean Energy by 2050. Technical Report. International Renewable Energy Agency (IRENA).
- Tona, P., Nguyen, H.-N., Sabiron, G., Creff, Y., 2015. An efficiency-aware model predictive control strategy for a heaving buoy wave energy converter. In: 11th European Wave and Tidal Energy Conference-EWTEC 2015.
- Trust, C., 2012. Carbon Trust Foreword to UK Wave Resource Study. Technical Report. Carbon Trust.
- Trust, C., 2014. Wave Energy Technology Brief. Technical Report. International Renewable Energy Agency (IRENA).

- Wang, H., Wijaya, V., Zeng, T., Zhang, Y., 2024. Deep reinforcement learning-based noncausal control for wave energy conversion. Ocean Eng. 311, 118860.
- Weiss, G., Li, G., Mueller, M., Townley, S., Belmont, M.R., 2012. Optimal control of wave energy converters using deterministic sea wave prediction. Fuel. Fut. Adv. Sci. Technol. Energy Gen. Transm. Storage 396, 29.
- Wächter, A., Biegler, L.T., 2006. On the implementation of an interior-point filter line-search algorithm for large-scale nonlinear programming. Math. Program. 106 (1), 25–57.
- Yu, S.-R., Zhang, M., Zhang, D.-Q., Yuan, Z.-M., 2024. Optimal declutching control of hinged multiple floating bodies. Ocean Eng. 306, 117992.
- Yu, Z., Falnes, J., 1995. State-space modelling of a vertical cylinder in heave. Appl. Ocean Res. 17 (5), 265–275.
- Zapf, B., Haubner, J., Kuchta, M., Ringstad, G., Eide, P.K., Mardal, K.-A., 2022. Investigating molecular transport in the human brain from MRI with physics-informed neural networks. Sci. Rep. 12, 15475.
- Zhan, S., Chen, Y., Ringwood, J.V., 2025. Computationally-efficient nonlinear model predictive control of wave energy converters with imperfect wave excitation previews. Ocean Eng. 319, 120125.
- Zhan, S., Li, G., 2019. Linear optimal noncausal control of wave energy converters. IEEE Trans. Contr. Syst. Technol. 27 (4), 1526–1536.
- Zhan, S., Stansby, P., Liao, Z., Li, G., 2023. A fast model predictive control framework for multi-float and multi-mode-motion wave energy converters. IEEE Trans. Contr. Syst. Technol. 31 (3), 1443–1450.
- Zhang, M., Yu, S.-R., Zhao, G.-W., Dai, S.-S., He, F., Yuan, Z.-M., 2024a. Model predictive control of wave energy converters. Ocean Eng. 301, 117430.
- Zhang, Y., Li, G., 2020. Non-causal linear optimal control of wave energy converters with enhanced robustness by sliding mode control. IEEE Trans. Sustain. Energy 11 (4), 2201–2209.
- Zhang, Y., Li, G., Al-Ani, M., 2024b. Robust learning-based model predictive control for wave energy converters. IEEE Trans. Sustain. Energy 15 (3), 1957–1967.
- Zhang, Y., Stansby, P., Li, G., 2021. Non-causal linear optimal control with adaptive sliding mode observer for multi-body wave energy converters. IEEE Trans. Sustain. Energy 12 (1), 568–577.
- Zhang, Y., Zeng, T., Li, G., 2020a. Robust excitation force estimation and prediction for wave energy converter m4 based on adaptive sliding-mode observer. IEEE Trans. Ind. Inf. 16 (2), 1163–1171.
- Zhang, Y., Zhan, S., Li, G., 2020b. Model predictive control of wave energy converters with prediction error tolerance. IFAC-PapersOnLine 53 (2), 12289–12294. 21st IFAC World Congress.
- Zheng, Y., Hu, C., Wang, X., Wu, Z., 2023. Physics-informed recurrent neural network modeling for predictive control of nonlinear processes. J. Process Contr. 128, 103005.
- Zou, S., Zhou, X., Khan, I., Weaver, W.W., Rahman, S., 2022. Optimization of the electricity generation of a wave energy converter using deep reinforcement learning. Ocean Eng. 244, 110363.